Available online at www.sciencedirect.com

ScienceDirect

IFAC Papers Online CONFERENCE PAPER ARCHIVE

IFAC PapersOnLine 52-21 (2019) 1–7

Hydrodynamic Performance of a Modular Biolocomotion Emulator

Hisham M. Shehata * **Craig A. Woolsey** **
Muhammad R. Hajj ***

* *Biomedical Engineering and Mechanics, Virginia Tech Blacksburg, VA 24061 USA (E-mail: hshehata@vt.edu)*
** *Aerospace & Ocean Engineering, Virginia Tech Blacksburg, VA 24061 USA (E-mail: cwoolsey@vt.edu)*
*** *Civil, Env., & Ocean Engineering, Stevens Institute of Technology Hoboken, NJ 07030 USA (E-mail: mhajj@stevens.edu)*

Abstract: This paper presents experimental measurements of the internal and external forces and moments generated during forced oscillation of a modular biolocomotion emulator executing four distinct gaits at three reduced frequencies and three Reynolds numbers (including zero). The purpose of the experimental program is to develop a database of hydrodynamic force measurements that can be used to validate low-order computational methods, such as the unsteady vortex lattice method, for design analysis.

Keywords: Hydrodynamics, thrust, propulsive efficiency, biolocomotion, towing basin

1. INTRODUCTION

The ability of a fish to deform its body in order to propel itself with desired speed, agility, maneuverability, and stability motivates the analysis and design of biomimetic underwater locomotion devices. There is a wide variety of pisciform (fish-like) morphologies and motion patterns ("gaits"), which are broadly classified according to how much of the body undulates to create propulsion. A boxfish, for example, uses "ostraciiform" locomotion in which the tail oscillates about a pivot point to generate propulsion. Jacks and mackarel are "carangiform" swimmers, undulating about one-third to one-half of their body length. Eels use "anguilliform" locomotion, in which nearly the entire body length undulates (Webb, 1975).

The notion of biomimetic autonomous underwater vehicles (AUVs) is not new and researchers have proposed a variety of designs over the years, from the simpler carangiform concepts (Kanso et al., 2005; Morgansen et al., 2007; Mason and Burdick, 2000) to those that more closely resemble snakes or eels (Liljebäck et al., 2012; Kelasidi et al., 2014; Kohl et al., 2016). Modeling efforts generally rely on analytical or semi-empirical quasisteady hydrodynamic approximations, even though these models are often inaccurate, particularly when considering the three-dimensional flow over a low aspect ratio device such as a robotic eel.

Detailed analyses of the morphologies and gaits in pisciform swimming, and the effects on the surrounding flow pattern, have helped scientists better understand the locomotion of fish. Consider, for example, a simple articulating hydrofoil which generates a sequence of shed vortices whose sense is reversed, relative to the familiar von Karman wake, so as to induce a jet in the direction of the mean flow. The propulsion force acting on the body is in reaction to this induced fluid momentum. It has also been shown that vortical energy can be recaptured from an incoming flow to minimize energy use during propulsion. The typical range of reduced frequencies in which significant thrust is produced is $k > 0.9$ (Eloy, 2012; Koochesfahani, 1989).

Like unsteady aerodynamic forces, the forces on an oscillating hydrofoil are transmitted by two primary mechanisms: added mass and circulatory effects. The force associated with added mass is purely a potential flow effect, independent of viscosity, which is a consequence of the fluid being accelerated around the body as the body moves through it. The circulatory force is associated with the introduction of vorticity into the flow by the hydrofoil. For a fish swimming at a high reduced frequency (highly unsteady flow), added mass effects are the dominant mechanism for force transmission (Weihs, 1989; Webb and Weihs, 1986).

Prior work has focused primarily on demonstrating prototypes in free swimming operation. This paper instead describes the planning and outcomes of captive motion experiments whose aim is to obtain and archive hydrodynamic force and moment data that can be used to validate reduced order computational methods such as the unsteady vortex lattice method (UVLM). The experimental program focuses on a particular biomimetic device, the modular biolocomotion emulator (MBE) described by Beardsley et al. (2018), which is forced to oscillate periodically while being towed in a straight line in calm water. The paper describes results for a test series in which the MBE was towed at two steady speeds (in addition to zero speed) while executing four distinct gaits at a variety of frequencies; the MBE geometry and kinematics can be varied further to test a broader range of morphologies and gaits. Although the primary focus of the effort is to generate data to validate computational models for

2405-8963
10.1016/j.ifacol.2019.12.274

design analysis, the paper also includes some analysis and interpretation of the experimental results.

2. EXPERIMENTAL SYSTEM

2.1 Test Article

The test apparatus used in this work is the *modular biolocomotion emulator (MBE)* described in (Beardsley et al., 2018). The MBE comprises a series of rigid components called modules. The device allows for the addition or removal of modules to represent various morphologies. In its simplest configuration, with a forebody and a single rigid fin, the MBE generates ostraciiform motion. With an additional link between the forebody and the fin, the MBE can generate a carangiform motion. The locomotion modality varies from oscillatory to undulatory as the number of modules grows, eventually approximating anguilliform locomotion. For the experiments described here, the MBE is configured to support experiments at the carangiform end of the locomotion spectrum. It comprises four modules: a forebody, two faired actuator modules, and a single rigid fin or tail.

The forebody of the MBE, which contains some of the MBE control electronics, is fixed to an immersible six degree-of-freedom (6DOF) balance suspended below a towing carriage. Each module contains a servo-actuator capable of applying a control moment to the subsequent module. Specifically, each module houses a waterproof SAVOX SW1210SG high torque servo, powered by a 7.4 VDC supply, to provide the oscillatory motion required of each module in order to effect a desired gait. These servos are capable of producing 800.0 N-cm of torque and slewing 60° in 0.13 seconds.

The fairings are 3-D printed using Abs-M30 material, and are designed to allow each module to rotate relative to its neighbors while preserving a nearly continuous external shape. The forebody geometry is the leading 70% of a NACA 0024 hydrofoil. The modules between the forebody and tail have a constant span. The tail fairing geometry is the trailing 30% of the NACA 0024 hydrofoil. A CAD model of the MBE can be seen in Figure 1 and a top view schematic of the MBE as configured for these experiments can be seen in Figure 2. The force and moment components F_x, F_y and M_z are measured using the 6DOF balance. The angles θ_1, θ_2 and θ_3 represent relative orientations for each module, which are affected by the servo control torques τ_1, τ_2 and τ_3. For additional details concerning the design of the MBE, its electronic instrumentation, or data acquisition, see (Beardsley et al., 2018).

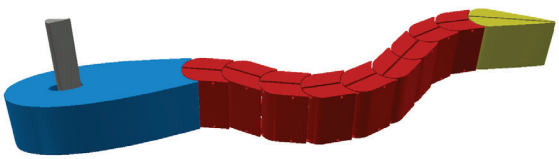

Fig. 1. Rendering of the assembled, multi-link MBE.

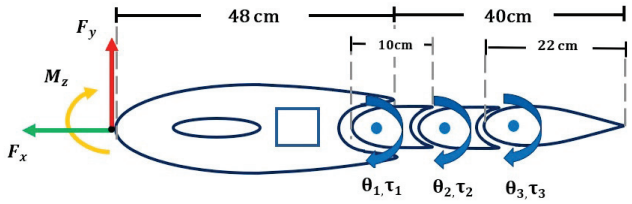

Fig. 2. Schematic of the MBE as tested (top view).

2.2 Test Facility

Measurements were obtained by towing the MBE from an instrumented towing carriage within the Virginia Tech Towing Basin. The basin is 30 m long, 1.8 m wide and 1.2 m deep. The carriage is driven by a 400 VDC motor and is capable of reaching towing speeds up to 3 m/s. The carriage speed, as indicated by a tachometer, is logged by the data acquisition system along with force and moment components from the 6DOF balance and various signals of interest within the MBE. Elements of the test facility are shown in Figure 3.

Fig. 3. Top: Towing carriage, control panel. Bottom: Installed MBE, towing tank

2.3 Data Acquisition System

The load cell used is the 6DOF SB-100 sting balance manufactured by Modern Machine & Tool Co. and shown in Figure 4. The sensor is connected to a box converter, also shown in Figure 4, which processes the strain gauge voltages to produce measurements of axial, normal, and side forces and of yaw, roll, and pitch moments. Only the horizontal plane components are recorded in these experiments: axial and side force and yaw moment. Calibration limits are 445 N in the axial force direction (x), 90 N in the lateral force direction (y), and 4,500 N-cm in the yaw moment direction (about z).

The axial force F_x, lateral force F_y, and yaw moment M_z on the MBE forebody are obtained from the 6DOF

Fig. 4. 6DOF Sting Balance SB-100 model (left), strain gauge box converter (right)

balance. Strain signals are then fed to a Vishay Micro-Measurements 2310 signal conditioning amplifier. All signals are conditioned using analog electronics and logged using LabVIEW. Data are acquired at 50 Hz from two devices: a National Instruments (NI) myDAQ and a Teensy 3.2 microcontroller. The NI myDAQ acquires axial force, side force, and yaw moment data from the balance while the Teensy 3.2 acquires position and torque measurements from each of the servos. Each module on the MBE contains its own Teensy 3.2 microcontroller, programmed using the Arduino integrated development environment (IDE). This Teensy microcontroller delivers command signals to the servo and reads two analog voltages from it. The first analog voltage, measured at the wiper of the servo's feedback potentiometer, indicates the servo's angular position. The second analog voltage, obtained from an ACS712 current sensor connected in series with the servo, provides a measurement of servo torque. Table 2.3 summarizes the input commands and output measurements for the experimental program.

Inputs	**Outputs**
Towing speed, U_∞ (m/s)	Axial and side forces, F_x and F_y
Tail frequency, f (Hz)	Yaw Moment M_z
Tail amplitude, A_P	Servo torques, $\tau_{1,\text{net}}, \tau_{2,\text{net}}, \tau_{3,\text{net}}$
Gaits, $\theta_1(t)$, $\theta_2(t)$, $\theta_3(t)$	Motion histories

Table 1. Experimental inputs and outputs

Within each module, the servo is powered directly from an 8.4 VDC bus while a voltage regulator provides 5.0 VDC to power the microcontroller and current sensor. All Teensy 3.2 microcontrollers within the MBE share a single I2C communication bus, which requires only two serial communication lines (clock and data). The microcontroller in the forebody serves as a master on the communication bus. This device communicates separately via USB with a LabVIEW script running on a laptop computer aboard the towing carriage. All data acquired are smoothed using a digital fourth-order Butterworth low-pass filter to attenuate high frequency noise above a cut-off frequency that is 4 times the frequency of the kinematic waveform.

2.4 Uncertainty Analysis

To estimate the uncertainty in signal measurements obtained from the strain gauges, servo angle potentiometers, and servo torque current sensors, a method similar to the one employed in Alam et al. (2010) is used. The load cell signal was captured for 10 seconds for three trials, corresponding to 1500 samples of data, and the distribution of the sample averages was obtained. The corresponding standard deviation (σ) was approximately 3.9% of the mean value. The 2σ value of $\pm 7.8\%$ indicates the F_x strain gauge measurement uncertainty at the 95% confidence level. The same technique are applied to estimate the sensor uncertainties in F_y, M_z, the servo torques, and the servo angles; these are $\pm 3.6\%$, $\pm 8.4\%$, $\pm 0.9\%$ and $\pm 3.4\%$, respectively.

Each servo's angular position is acquired from the wiper voltage of the servoactuator's potentiometer, sampled at 50 Hz. The analog voltage is converted to angular position (in degrees) using a previously calibrated curve fit. A time delay is set by the microcontroller's clock input which commands a signal to drive the servo at a given frequency, producing an uncertainty in frequency inputs of ± 0.005 Hz. The frequency input to each servo is verified by examining the Fourier transform of the potentiometer measurements.

2.5 Test Matrix

The particular motion exhibited by the device, as defined by the periodic waveforms that each of its actuators generates, is referred to as the "gait." The gait is defined by the fundamental waveform shape (sinusoidal, triangular, etc.), the frequency of oscillation of the modules, and the amplitude of oscillation of the MBE's trailing edge.

To attain a desired gait, the servo-actuator within each module executes a prescribed motion history. Briefly, one determines the servo angle histories that best approximate the given gait for a given number of modules (three, in this case) by solving a system of nonlinear algebraic equations for the position of each servo. We consider four gaits: a sinusoidal wave, a "rigid pitching" gait, and two gaits which approximate a simple 1st and 2nd bending mode, respectively. For the sinusoidal wave, the angle input for each servo is determined by the amplitude of the sine function. For the rigid pitching gait, in which the modules all move in rigid unison, every servo outputs the same angle relative to the first module. As for the 1st and 2nd bending modes, the servo angles are determined by solving the Euler-Bernoulli beam equation. A schematic of these four gaits is shown in Figure 5. The prescribed servo angles (relative to the x-axis frame) for each waveform are presented in Figure 6.

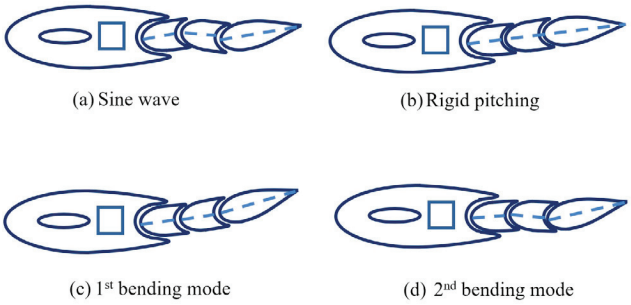

Fig. 5. Schematic representation of the four swimming gaits for MBE testing.

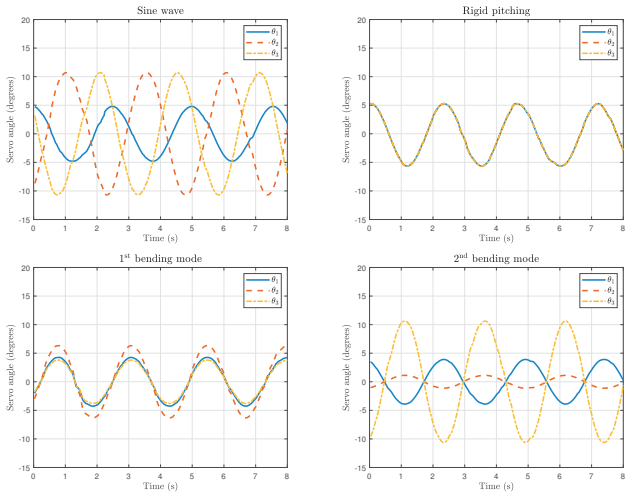

Fig. 6. Servo angle inputs for sine wave (top left), rigid pitching (top right), 1st bending mode (bottom left) and 2nd bending mode (bottom right). θ_1: solid blue, θ_2: red dashed, θ_3: orange dashed-dot.

Two test cases are considered:

- **Case A** - The MBE modules oscillate without forward motion ($U_{\text{ref}} = 0$). In this case, the measured forces and moment are purely those generated by the lateral accelerations of the components, that is, the apparent mass.
- **Case B** - The MBE modules oscillate while the apparatus moves forward in the x-direction at a steady speed ($U_{\text{ref}} = U_\infty > 0$).

The forces and moment for Case A are direct measurements. For Case B, the force F_y and moment M_z are also direct measurements, but the axial force F_x is the computed *difference* between the measured axial force $F_{x,\text{net}}$ and the drag force D_{body} for the unactuated device at the given steady towing speed:

$$F_x = F_{x_{\text{net}}} - D_{\text{body}} \tag{1}$$

To determine the hydrodynamic torque $\tau_{i,\text{H}}$ associated with each element aft of the forebody, the mechanical torque $\tau_{i,\text{M}}$ produced by each servo when generating the given gait *in air* is subtracted from the net torque $\tau_{i,\text{net}}$ that is directly measured during the experiment for each of the three elements:

$$\tau_{i_{\text{H}}} = \tau_{i_{\text{net}}} - \tau_{i_{\text{M}}} \quad \textbf{for} \quad i = 1, 2, 3 \tag{2}$$

The two intermediate modules and tail, together with the forebody, yield an overall body length of 88 cm. The vertical tail amplitude A_p is measured from the tip of the tail's maximum stroke position relative the centerline of the forebody; A_p is predetermined by measuring the tail peak amplitude against gait inputs provided by LabVIEW. The tail peak amplitudes for all four gaits are tuned so that they measure 4 cm. A summary of the various MBE configurations and dynamic operations is given in Table 2.

3. RESULTS AND DISCUSSION

The experiments outlined in Table 2 were performed in April 2019, yielding data sets for three distinct trials.

Parameter	**Value(s)**
Towing speed, U_∞ (m/s)	$0.13, 0.23$
Reynolds No, Re ($\times 10^5$)	$1.40, 2.33$
Reduced Frequency k	$5.2, 7.7, 10.2$
Frequency, f (Hz)	0.25, 0.38, 0.42, 0.5, 0.63, 0.83
Tail peak amplitude, A_P	≈ 4.0 cm $\pm 1.25\%$
Waveforms (gaits)	sine wave, rigid pitching 1st and 2nd bending modes

Table 2. Experiment conditions for testing

While it would be impractical to present a comprehensive review of the experimental results, this section provides (1) a discussion of the data associated with one representative subset of test conditions and (2) summary plots of axial force data for all test conditions. In the former case, the selected test condition corresponds to an MBE waveform frequency of 0.42 Hz and two Reynolds numbers: 0 and 2.33×10^5. All experimental data have been archived and are publicly accessible. [1]

3.1 Static Force Measurements

Figure 7 shows the body drag force generated when towing the unactuated MBE at three different towing speeds. When actuated, the device produces a net axial force that is the thrust minus the body drag. It is difficult or impossible to separate these two components, in practice. Regardless, it is most appropriate to compare the *net* thrust that is generated by the oscillating MBE with the unactuated drag force, as the latter is the *least* resistance that would be encountered when propelling the device by more conventional means.

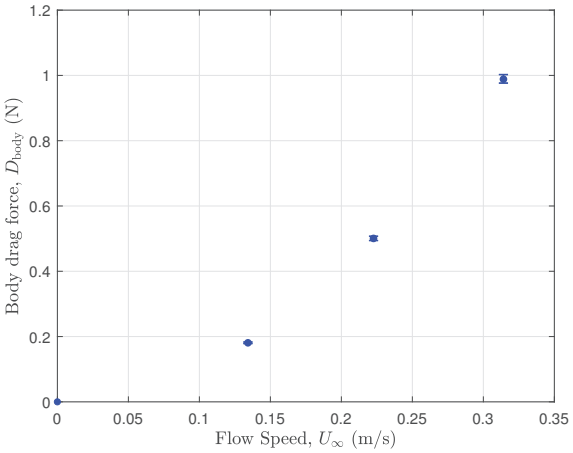

Fig. 7. Body drag force vs freestream velocity

3.2 Dynamic Force Measurements

The top half of Figure 8 shows time histories of axial force, side force and yaw moment for Case A. Recall that there is no forward motion, in this case; the results show the force and moment components generated purely by the apparent mass of the oscillating members. The bottom half of Figure 8 shows a sample of time histories of axial force, side force and yaw moment for Case B. In this case, the freestream velocity is $U_\infty = 0.13$ m/s.

[1] https://sites.google.com/a/vt.edu/biomimetic-locomotion/

In both cases, the sine wave kinematics generate force and moment components with the lowest amplitude. The rigid pitching gait produces the largest amplitude, which is consistent for all test conditions. Between the 1st and 2nd bending mode kinematics, the amplitudes of the responses show little difference in Case A, but larger response amplitudes were noted for the 2nd bending mode kinematics in Case B. For all gaits, Case B results in force responses larger than those in Case A. The flow dynamics in Case B involve a combination of added mass, circulation, rotation, viscosity and 3-D effects. As a result, the time histories in Case B exhibit stronger nonlinear fluctuations.

We define the non-dimensional *reduced frequency*

$$k = \frac{\pi f c}{U_{\text{ref}}} \tag{3}$$

where U_{ref} is a reference speed (the tail tip velocity U_{tip} for Case A and the free stream velocity U_∞ for Case B), f is the tail oscillating frequency, and c is a characteristic length, the overall length of the MBE (88 cm).

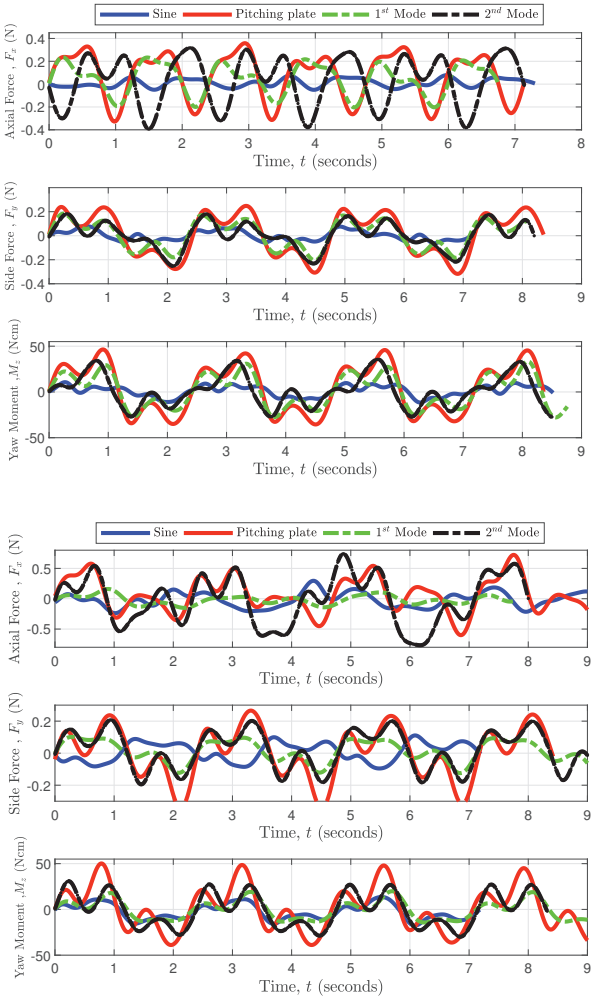

Fig. 8. Force response for four gaits at flapping frequency f=0.42 Hz. Case A: Reynolds number, $Re = 0$ (top) and Case B: Reynolds number, $Re = 2.33 \times 10^5$ (bottom).

In the top half of Figure 9, where the towing speed is zero, note that thrust and torque increase with forcing frequency for the sine wave and the 2nd bending mode kinematics over the range of frequencies tested. For the rigid pitching and 1st bending mode gaits, however, the thrust appears to peak within the range of excitation frequencies.

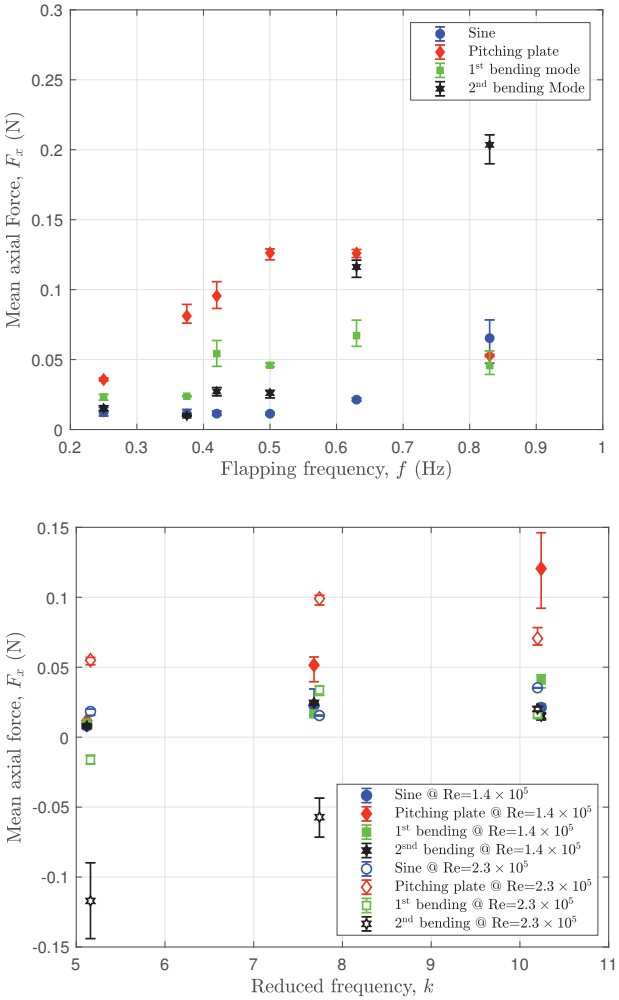

Fig. 9. Mean axial forces for all test conditions. Case A: Reynolds number, $Re = 0$ (top) and Case B: Both nonzero Reynolds numbers (bottom).

As discussed earlier, the shedding of a vortex by an oscillating hydrofoil, within a particular range of reduced frequencies, reverses the rotational direction of the von Karman vortices and induces a jet-like flow in the direction of the free stream. This is one of the main sources of forward propulsion. Thrust production by a fish also depends on its morphology and swimming movements. The trailing edge vortices are usually accompanied by a moderately strong leading edge vortex, usually generated when the forebody of the fish is at a high angle of attack. The forebody of the MBE is fixed at zero angle of attack, so it is unlikely to generate a leading edge vortex. However, the lateral excursions of the faired modules downstream of the forebody may yield additional shed vortices which serve a similar role to a leading edge vortex in helping to generate forward thrust. The strength of the flow momentum created by the jet created by a flapping hydrofoil depends on the incoming flow speed and the strength of the vortices. The incoming

flow speed significantly affects the flow-induced force on an object (Quinn et al., 2014). The effects of the vortices are determined by the proximity of shed vortices to the aft body of the flapping device. The higher the flow speed is, the quicker these vortices advect downstream, resulting in a weaker jet and a lower propulsive reaction force.

The 1st and 2nd bending mode kinematics generate lower mean axial forces at higher Reynolds numbers and lower frequencies. In general, for Case B (nonzero mean flow), all vortices shed from the tip of the tail are advected away from the wake. The rate of advection is high at higher free stream velocities. Since all waveforms produce similar tail tip amplitudes A_p, the gait results in shed vortices around the appendages which may either enhance or diminish the net thrust. In fact, at lower frequencies, the 1st and 2nd bending modes produce negative thrust. This indicates another source of drag in addition to the drag created by the forebody itself. This additional drag may be due to wake drag created by large lateral excursions of MBE modules for particular gait parameters. The rigid pitching gait should also yield low thrust forces for Case B, as this gait has the largest lateral excursions. However, this gait also produces added mass forces sufficient to overcome the additional drag.

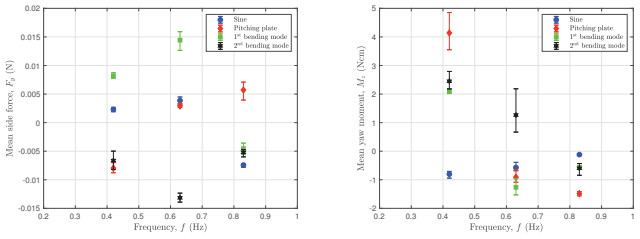

Fig. 10. Mean side forces (left) and yaw moments (right) for Case A test conditions. Sine wave: blue circle; rigid pitching: red diamond; 1st bending mode: green square; 2nd bending mode: black star

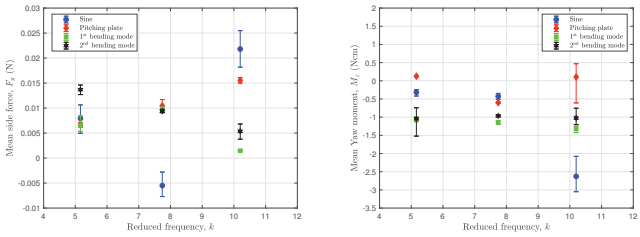

Fig. 11. Mean side forces and yaw moments for Case B test condition at $Re = 2.33 \times 10^5$. Sine wave: blue circle; rigid pitching: red diamond; 1st bending mode: green square; 2nd bending mode: black star

Figures 10 and 11 present the mean values for the measured side force and yaw moment generated by the MBE at Reynolds numbers of zero and 2.3×10^5. Relatively large positive or negative mean values can provide some insight concerning the resultant motion of a freely swimming biological or biomimetic agent. Note that, despite the fact that the device flaps symmetrically in the "upstroke" and "downstroke," some gaits exhibit significant asymmetric force response. Over a range of frequencies, the vortex street generated can deviate away from the center line of the forebody (Anderson et al., 1998; Koochesfahani, 1989), resulting in non-zero side forces and yaw moments. Even for a fully developed wake, the structure of the vortex street formed is highly dependent on frequency of oscillation, gait motion and freestream flow speed, and can drastically change the overall forces acting on the body.

There are substantial differences between the results presented in zero and non-zero freestream. With no freestream flow, the oscillating tail does not generate the same pattern of shed vortices that is observed in a steady, non-zero freestream. The lateral and streamwise spacings of the vortices formed can differ for the two cases, even for the same waveform input. Also, the side force and yaw moment histories suggest the formation of leading edge vortices over the faired modules while executing the waveforms. For the 2nd bending mode waveform, at a Reynolds number of 2.3×10^5, a positive mean side force results, whose magnitude decreases with increasing frequency; this same waveform generates a negative mean side force at $Re = 0$. For a rigid pitching waveform, on the other hand, the mean side force increases with increasing frequency at both Reynolds numbers. Also, a substantial mean yaw moment arises for both Reynolds numbers.

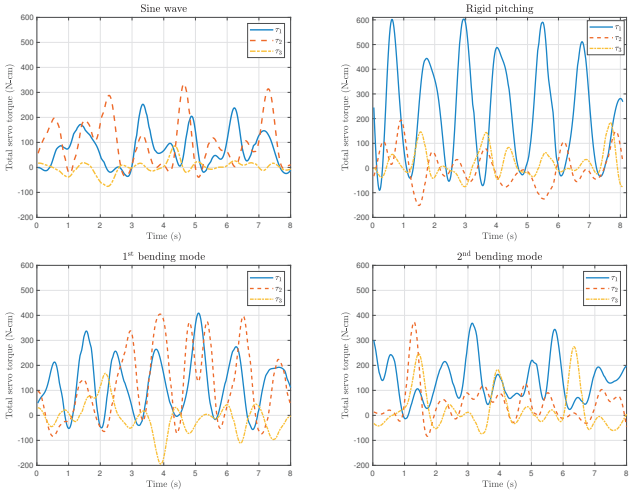

Fig. 12. Servo torque outputs for sine wave (top left), rigid pitching (top right), 1st bending mode (bottom left) and 2nd bending mode (bottom right). τ_1: solid blue, τ_2: red dashed, τ_3: orange dashed-dot.

Figure 12 shows servo torque measurements for the three MBE modules aft of the forebody for all four gaits at an oscillation frequency of 0.42 Hz. These torque measurements are instantaneous and represent the net torque, $\tau_{i_{\text{net}}}$, required to move the module fairings against hydrodynamic resistance loads. The torques exerted by servos 1 and 2 are generally commensurate and larger than that exerted by servo 3. Rigid flapping is an exception, where servo 1 exerts a far larger control torque, consistent with intuition.

4. CONCLUSION AND FUTURE WORK

A modular biolocomotion emulator (MBE) designed to generate validation data for reduced order computational models of unsteady hydrodynamic forces and moments in biological and biomimetic swimmers has been tested in the Virginia Tech Towing Basin. The experimental

program provides quantitative information about the hydrodynamic forces and moments generated as a result of particular waveforms (gaits) and Reynolds numbers over a range of steady towing speeds. This paper presents an overview of the experimental results obtained using the MBE, which can inform the analysis and design and biomimetic swimming vehicles.

Beyond simply collecting and archiving data for future use, these experiments also provide some insight concerning the hydrodynamic force and moment response of a biomimetic device to different gaits, with implications for the design analysis of multibody underwater robots. Detailed hydrodynamic analysis and validation of UVLM computations are continuing research efforts.

There are several potential avenues for future work. For example, the MBE can be extended to include more modules, enabling the simulation of gaits at the anguilliform end of the locomotion spectrum. Also, using feedback control of the internal torques within the MBE, one can artificially produce various hydroelastic properties, so that the device can support the study of flexibility effects and hydroelastic tailoring.

ACKNOWLEDGEMENTS

The authors kindly acknowledge the support of the National Science Foundation (NSF) under the Grant No. CMMI-1635143. The authors also gratefully acknowledge the help provided by the following undergraduate research assistants: Ahmed Nayfeh, Alex Mclean, Charles Watson, Colton Beardsley, Khanh Nguyen, Luke Bergeron, Matthew Young and Minh Vu.

REFERENCES

Alam, M.M., Zhou, Y., Yang, H., Guo, H., and Mi, J. (2010). The ultra-low reynolds number airfoil wake. *Experiments in fluids*, 48(1), 81–103.

Anderson, J., Streitlien, K., Barrett, D., and Triantafyllou, M. (1998). Oscillating foils of high propulsive efficiency. *Journal of Fluid Mechanics*, 360, 41–72.

Beardsley, C., Bergeron, L., McLean, A., Nguyen, K., Vu, M., Watson, C., Nayfeh, A., Shehata, H., Woolsey, C., and Hajj, M. (2018). A modular biolocomotion emulator for hydrodynamic testing in a towing tank. In *OCEANS 2018 MTS/IEEE Charleston*, 1–8. IEEE.

Eloy, C. (2012). Optimal strouhal number for swimming animals. *Journal of Fluids and Structures*, 30, 205–218.

Kanso, E., Marsden, J.E., Rowley, C.W., and Melli-Huber, J.B. (2005). Locomotion of articulated bodies in a perfect fluid. *Journal of Nonlinear Science*, 15(4), 255–289.

Kelasidi, E., Pettersen, K.Y., Gravdahl, J.T., and Liljebäck, P. (2014). Modeling of underwater snake robots. In *2014 IEEE International Conference on Robotics and Automation (ICRA)*, 4540–4547. IEEE.

Kohl, A.M., Pettersen, K.Y., Kelasidi, E., and Gravdahl, J.T. (2016). Planar path following of underwater snake robots in the presence of ocean currents. *IEEE Robotics and Automation Letters*, 1(1), 383–390.

Koochesfahani, M. (1989). Vortical patterns in the wake of an oscillating airfoil. *AIAA Journal*, 27(9).

Liljebäck, P., Pettersen, K.Y., Stavdahl, Ø., and Gravdahl, J.T. (2012). *Snake robots: modelling, mechatronics, and control*. Springer Science & Business Media.

Mason, R. and Burdick, J.W. (2000). Experiments in carangiform robotic fish locomotion. In *Robotics and Automation, 2000. Proceedings. ICRA'00. IEEE International Conference on*, volume 1, 428–435. IEEE.

Morgansen, K.A., Triplett, B.I., and Klein, D.J. (2007). Geometric methods for modeling and control of free-swimming fin-actuated underwater vehicles. *IEEE Transactions on Robotics*, 23(6), 1184–1199.

Quinn, D.B., Lauder, G.V., and Smits, A.J. (2014). Scaling the propulsive performance of heaving flexible panels. *Journal of fluid mechanics*, 738, 250–267.

Webb, P.W. (1975). Hydrodynamics and energetics of fish propulsion. *Bulletin of the fisheries research board of Canada*, 190, 1–159.

Webb, P.W. and Weihs, D. (1986). Functional locomotor morphology of early life history stages of fishes. *Transactions of the American Fisheries Society*, 115(1), 115–127.

Weihs, D. (1989). Design features and mechanics of axial locomotion in fish. *American Zoologist*, 29(1), 151–160.